J. Fluid Mech. (1994), *vol.* 258, *pp.* 1–29

Low-dimensional description of free-shear-flow coherent structures and their dynamical behaviour

By MOJTABA RAJAEE, STURE K. F. KARLSSON AND LAWRENCE SIROVICH

Center for Fluid Mechanics and the Division of Engineering, Brown University, Providence, RI 02912, USA

(Received 16 June 1992 and in revised form 28 May 1993)

The snapshot form of the Karhunen–Loève (K–L) expansion has been applied to two-dimensional, two-component hot-wire data from the region of a weakly perturbed free shear layer that includes the first pairing process. Low-level external perturbation was provided by a loudspeaker driven by a computer-generated signal composed of two sine waves of equal amplitude at the frequencies of the naturally developing fundamental instability wave and its first subharmonic, separated by a controllable initial phase angle difference. It was found that a large fraction of the fluctuation energy is carried by the first few modes. A low-dimensional empirical eigenfunction space is obtained which describes the shear-flow coherent structures well. Galerkin projection of the Navier–Stokes equations onto this basis set of principal eigenfunction modes results in a low-order system of dynamical equations, and solution of this system of equations describes the dynamics of the coherent structures associated with eigenfunctions. Finally the simulation, as obtained from the system of dynamical equations, is shown to compare reasonably well with the experiments.

1. Introduction

Large-scale coherent structures in free shear layers have been the subject of many studies (see Ho & Huerre 1984 for a comprehensive review) owing to their important role in mixing, entrainment and the laminar–turbulent transition processes. Large-scale coherent vortical structures were first observed by Brown & Roshko (1974) using a flow visualization technique, and their role in the entrainment process was investigated using flow visualizations by Dimotakis & Brown (1976). Further studies by Winant & Browand (1974), using flow visualizations, Browand & Wiedman (1976), using conditional sampling of detector probes, and Ho & Huang (1982), using conditional sampling and flow visualizations, provided comprehensive experimental information on the pairing mechanism of these large-scale structures.

In our laboratory, Yang & Karlsson (1991) employed a phase-locked conditional sampling technique by using the subharmonic component of the driving signal as a timing reference for phase averaging of the hot-wire data at specific phases of the driving signal. They were able to use the time-sequence conditionally sampled data to demonstrate two distinct types of vortex interaction, pairing and tearing, depending on the driving phase angle difference between the subharmonic and the fundamental frequency components of the driving signal. However, the fluctuation field of the disturbances at the frequencies which are not harmonics of the subharmonic instability mode, as well as the contribution from the irregularities such as phase jitter, were averaged out by the phase-averaging technique.

Later work (Rajaee & Karlsson 1992), using a Fourier space decomposition of the free-shear-flow measurements, revealed the relation between the measured data in the frequency space and the evolution of large-scale vortical structures. We were able to show that relatively few instability modes contain most of the fluctuation energy. However, downstream of the first pairing event, the flow tends to become chaotic in a manner involving phase jitter and higher-frequency fluctuations. Because of the phase jitter, difficulties arise in the use of phase averaging and Fourier methods. Use of the Karhunen–Loève decomposition was found to overcome the deficiencies of the former methods in handling the more chaotic stages of the flow (Rajaee 1991). By this method one does not have to impose any condition on sampling the data or discard any information. In other words, the results are not filtered in any way. The only constraint involved depends on the percentile of energy of the fluctuation field one wants to recover. This method provides a means of studying the non-coherent structures of the flow, including the jitters and small-scale structures, and their relation to the large-scale coherent structures. It provides information on the origin of their development and growth as well as their energy contribution. This method results in saving the entire flow field information in a basis set of eigenfunctions and their corresponding dynamical coefficients, or a system of dynamical equations, from which the flow field can be easily reconstructed for different initial conditions. This results in a means of control and management of the flow.

The K–L expansion has been applied to a variety of problems in different fields for decades (see Preisendofer 1988; Sirovich 1991; and Sirovich & Everson 1992 for early references). Its application to problems involving fluids goes back to Fukuoka (1951), Lorenz (1956) and White *et al.* (1958), and it is known under the name of *empirical orthogonal functions* in statistical weather forecasting. Later, this method was employed for the combined representation of three climatic variables and referred to as the *empirical eigenvectors* by Kutzbach (1967). Lumley (1967) suggested that the procedure might be used in fluid mechanics to quantify the notion of coherent structures. The basic idea is that spatial velocity correlations be orthogonally decomposed as a rational and quantitative method of identifying coherent structures which leads to the eigenfunction-eigenvalue problem,

$$\int R_{ij}(x, x')\,\phi_j^n(x')\,\mathrm{d}x' = \lambda^{(n)}\phi_i^{(n)}(x), \tag{1}$$

where the kernel, $\boldsymbol{R}$, is the two-point correlation matrix

$$R_{ij}(x, x') = \overline{u_i(x)\,u_j(x')}, \tag{2}$$

and $\phi^{(n)}(x)$ are the eigenfunctions representing the structures of the organized motions. This way of extracting organized structures is based upon an energy-weighted measure; that is, the structures are those that contribute most to the energy. This representation is known in the literature of probability theory as the 'proper orthogonal decomposition theorem' (Loève 1955; Lumley 1981). In pattern recognition, it is known as the Karhunen–Loève expansion (Ash 1975; Fukunaga 1972) and as factor or principal-component analysis in the statistical literature (Ahmed & Goldstein 1975).

This method has been applied to a number of problems in turbulent flow, including boundary-layer flow by Bakewell & Lumley (1967), wake flows by Payne & Lumley (1967) and the numerical simulation of turbulent channel flows by Moin (1984). It has been applied to experimental data information of a turbulent jet mixing layer by Glauser, Lieb & George (1985) as well as of the near-wall region of turbulent pipe flow (Herzog 1986). It has also been applied to a forced mixing layer (Glezer, Kadioglu &

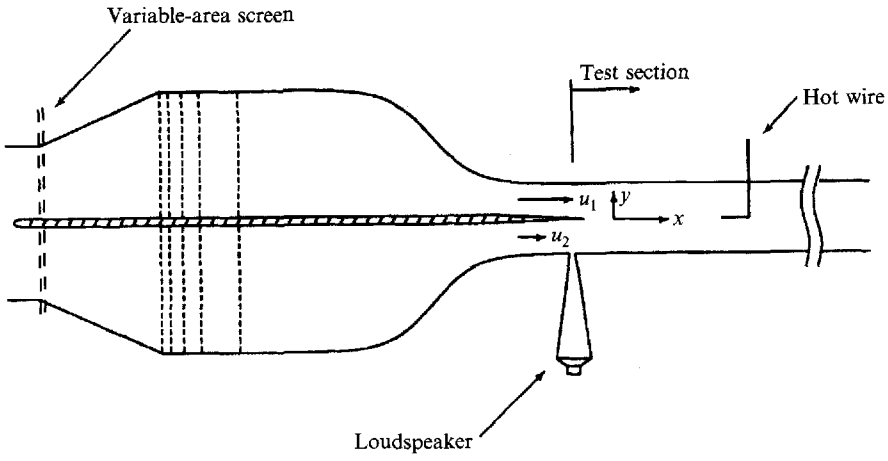

FIGURE 1. Sketch of flow system.

Pearlstein 1989). They have extended the method of proper orthogonal expansions to deal with statistically non-stationary flows and applied it to a time-periodically forced plane mixing layer.

A new perspective for the use of the K–L expansion in fluid dynamics is presented in Sirovich (1987*a–c*) where it suggested that it be used as a basis for low-dimensional dynamical approximations. This series of papers discusses the mathematical basis of the K–L decomposition and develop the *method of snapshots* for obtaining a complete set of orthonormal empirical eigenfunctions which meet the boundary conditions and appropriate side conditions. Procedures for developing a system of dynamical equations, employing the eigenfunctions obtained, to follow the turbulent evolution of the flow have been presented (Sirovich 1987*a–c*, 1989). Sirovich & Rodrigues (1987) used this approach to show that low-dimensional dynamics could be achieved for chaotic motions governed by the Ginzburg–Landau equation over a wide parameter set. In an independent study Aubry *et al.* (1988) applied similar ideas to the study of the near-wall region of turbulent pipe flow using the experimentally determined eigenfunctions of Herzog (1986). Sirovich, Kirby & Winter (1990) applied the K–L procedure to the analysis of digitally imaged two-dimensional gas concentration fields obtained for a seeded axisymmetric jet. It has also been applied to turbulent thermal convection (Sirovich, Maxey & Tarman 1987) as well as to low-dimensional descriptions of other complicated phenomena (Sirovich & Sirovich 1989). Kawakubo (1990) also applied the K–L expansion to the direct simulation result of a turbulent mixing layer with substantial agreement with our earlier results (Rajaee & Karlsson 1990).

We use the snapshot form of the Karhunen–Loève procedure for analysing the hot-wire free-shear measurements in order to describe the flow structures in terms of a low-dimensional basis set of empirical eigenfunctions. This basis set will then be used to develop a low-dimensional system of dynamical equations. The solution of this system of dynamic equations will be compared with the direct projections of flow realizations on this basis set of eigenfunctions. The good agreement of the solution of the system of dynamical equations with the direct projection results is a promising indication that the dynamical equations may be used to explore the turbulent evolution of the flow.

2. Experimental facilities and procedure

2.1. *Experimental facilities*

The experimental set-up is the same as the one described in the recent paper by Rajaee & Karlsson (1992). A closed-return low-speed wind tunnel, a portion of which is sketched in figure 1, is used to provide a free-shear-layer experimental facility. The flow is divided into two streams of high- and low-speed sections by a splitter plate, extending throughout the settling and contraction chambers, with its sharp trailing edge at the beginning of the test section. The high and low speeds are controlled by adjusting the variable-density screens, located at the leading edge of the splitter plate. The mean velocity of the high- and low-speed streams, U_1 and U_2, are chosen as 5.8 and 3.0 m/s, respectively. The velocity ratio, defined as $R = (U_1 - U_2)/(U_1 + U_2)$, is then 0.32. The momentum thickness of the shear layer where the wake of the splitter plate has just disappeared is $\theta_0 = 0.99$ mm, based on the definition of

$$\theta = \frac{1}{(U_1 - U_2)^2} \int_{-\infty}^{+\infty} (U_1 - U(y))(U(y) - U_2)\,\mathrm{d}y$$

by Huang & Ho (1990). The natural instability frequency in our experiment, with the above high and low free-stream velocities and the initial momentum thickness θ_0, is 136 Hz, as predicted by the linear theory (Monkewitz & Huerre 1982; Michalke & Hermann 1982). The corresponding natural instability wavelength is measured as $\lambda_0 = 3.25$ cm. The flow Reynolds number based on half the sum of the free-stream velocities and half the initial maximum shear thickness on the high-speed side, $\delta_0 = 1.25$ mm measured at $X = 2$ mm downstream of the splitter plate edge, is approximately 360. The internal dimensions of the test section are 57 cm high, 81 cm wide, and 380 cm long. The horizontal splitter plate divides the inlet area into two equal sections. Careful design of the new settling chamber has provided a low initial turbulence level of 0.03% of the higher free-stream velocity. As discussed in the previous paper, this free shear flow is predominantly two-dimensional.

Two-dimensional excitation of the shear flow is achieved by acoustic means. A single 8 in. diameter loudspeaker, connected by a constant-cross-sectional-area transition piece to a transverse slot in the floor at the beginning of the test section is capable of generating two-dimensional disturbances of any desired frequency in the range of interest. The speaker is driven by a computer-generated signal consisting of two superimposed sine waves: the fundamental, which equals the unstable natural frequency, and its first subharmonic with a desired phase difference. Two-dimensionality of the generated perturbation was examined by velocity correlation measurements between a stationary probe at the centre of the trailing edge of the splitter plate, $X = 1$ cm, $Y = 2$ mm, $Z = 0$, and a probe traversing in the Z-direction. The correlation coefficient dropped to 0.70 at $Z = 20$ cm. It should be kept in mind that the fluctuation level at this X-location is very low. With a low-pass filter with the cut-off at 40 Hz this correlation became 0.85, corresponding to a phase shift in the imposed perturbation of approximately 32°. With a loudspeaker driving r.m.s. voltage amplitude of 1.5 V, the observed r.m.s. velocity fluctuation level at the trailing edge of the splitter plate was measured to be 0.4% of the average of the free-stream velocities. One X-probe hot-wire anemometer is used which can be traversed in both streamwise and transverse directions with a spatial resolution of 0.0005 in.

Following our previous work one experiment is done for the case of distinct pairing vortex interaction, i.e. corresponding to the initial phase angle difference of 270°

between the subharmonic and the fundamental sine-wave components of the driving signal, which is found to be suppressing the flow three-dimensionality.

2.2. *Composite snapshots*

The measurements are made between $X = 10$ and 35 cm and between $Y = 6$ and -6 cm in 1 mm intervals for both directions at the total of (251×121) locations. At each location $\frac{2}{10}$ of a second of data are taken from the X-probe hot wires as well as the subharmonic component of the driving signal at the sampling rate of 3060 s^{-1}, a multiple of 68 Hz which is the frequency of the subharmonic component of the driving signal. The high sampling rate is required to increase the accuracy, but we are constrained by the large disk space requirement, since a certain length of time should be covered, for storing the data for further processing. If sufficient number of data points with a fine time interval between them are used, most of the events due to the motion of coherent and non-coherent structures can be captured and this is the important issue that has been considered in this experiment. At each location data acquisition starts at a reference time, i.e. the zero crossing with the positive slope on a cycle of the subharmonic component of the driving signal, and continues for $\frac{2}{10}$ of a second, equivalent to more than 12 periods of the subharmonic component of the driving signal.

There is a maximum inaccuracy of 1/3059, i.e. less than 3×10^{-4} s, in the start of data acquisition which is corrected by interpolating and shifting the data points for the right starting time. The correction scheme is based on the following.

Consider the subharmonic component of the driving signal, which is a sine wave. The optimal start of the data acquisition is the exact time of zero crossing. However, there may not be a data point sampled at that specific time. Figure 2 shows the sampled subharmonic component of the driving signal and the corresponding hot-wire signal at the location of $X = 35$ cm and $Y = 0$, both collected at the same time. Consider E_2^o to be the hot-wire signal after the zero crossing time, E_1^o the hot-wire signal before the zero crossing and the corresponding sampled values for the subharmonic component of the driving signal to be r_2^o and r_1^o, respectively. At the zero crossing time, one could interpolate for the value of the hot-wire signal, E^o, from the following relation:

$$\frac{E_2^o - E^o}{E_2^o - E_1^o} = \frac{r_2^o - r^o}{r_2^o - r_1^o}, \tag{3}$$

where $r^o = 0$, the zero crossing of the driving signal's subharmonic component. Thus,

$$E^o = E_2^o - \frac{r_2^o}{r_2^o - r_1^o}(E_2^o - E_1^o). \tag{4}$$

Therefore, all the sampled data points must be shifted back by a correction factor, to reduce the formerly mentioned inaccuracy of the starting time of data acquisition. The correction factor is $Cr = r_2^o/(r_2^o - r_1^o)$ times the difference of the current measured value, which needs to be shifted, and the measured value at the preceding sampling time, i.e.

$$E^o = E_2^o - Cr(E_2^o - E_1^o). \tag{5}$$

In figure 2(*a*) one may note some lack of periodicity at the subharmonic frequency. We should remember that hot-wire measurements in this plot must first be corrected by the above-mentioned scheme for the experimental error at the zero crossing of the driving signal (figure 2*b*). The observed lack of periodicity is most revealing at the zero crossing phase. These sample measurements are made at the most sensitive location in

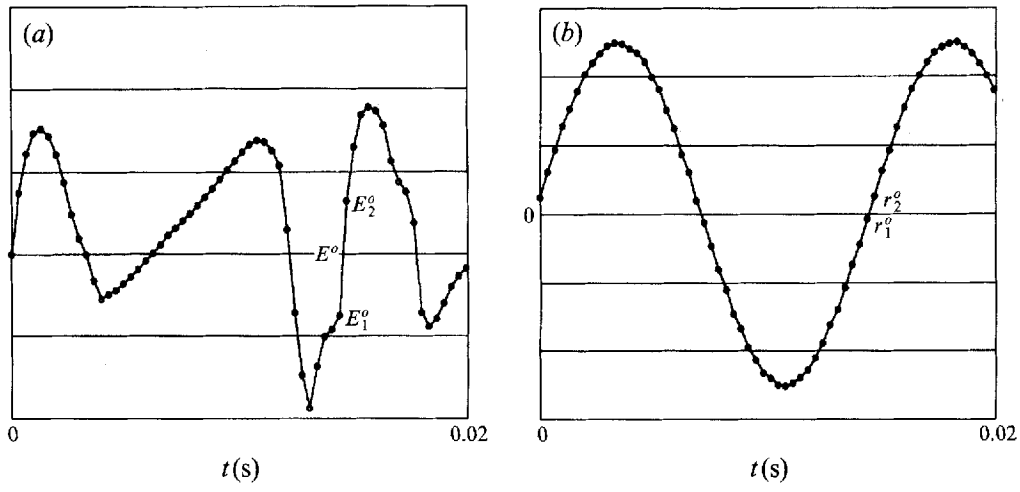

FIGURE 2. (*a*) Hot-wire measurements at $X = 35$ cm, $Y = 0$, and (*b*) the sampled subharmonic component of the driving signal, illustrating the concept of conditional sampling for producing the composite snapshots.

the flow region where there are growing irregularities in the flow due to phase jitter and small-scale structures which start developing in the pairing region. Also, it should be kept in mind that there are contributions from other instability modes than the subharmonic mode, as well as high-frequency fluctuations superimposed on the subharmonic mode, which cause the hot-wire data to appear to have a lack of periodicity at the subharmonic frequency. At $X = 35$ cm, $Y = 0$, the cross-correlation between the subharmonic component of the driving signal and the velocity fluctuations is about 0.8 at the zero crossing and very close to 1 at the maximum, or minimum, amplitude phase of the subharmonic component of the driving signal, using the short time measurements. This estimate reveals the extent of phase locking at the most dangerous location in the flow region under consideration.

Assuming flow stationarity in a time frame, phase locked with the driving signal, composite snapshots are produced using the data acquired in the above-mentioned time frame (Rajaee & Karlsson 1990). Corresponding to each specific time, or phase, there is a composite snapshot of the flow field starting at t_0, the start of data collection at the formerly mentioned zero crossing time. The continuity is checked by comparing the inflow and the outflow from all the boundaries of the flow region between any two streamwise locations. The difference between the inflow and the outflow, for any flow region between any two streamwise locations, is normalized with the inflow from the left cross-section of the flow region at $X = 10$ cm downstream of the splitter-plate trailing edge. The difference of outflow and inflow is at most 1.1%; that is, the accuracy in satisfying the two-dimensional continuity equation is at least 98.9%. Therefore, composite snapshots prove to satisfy the two-dimensional continuity equation with a high accuracy, a necessary condition to regard them as possible representations for an appropriate instantaneous one.

The composite snapshots are equal to the instantaneous ones for the purpose of extracting the large-scale coherent flow structures. Here, 540 composite snapshots, equivalent to the number of samples taken in 12 cycles of the subharmonic wave, are considered for the eigenvalue problem, equation (1). The streamwise extent of the flow field studied is about four wavelengths of the subharmonic instability wave. Therefore, the number of snapshots being used is generously sufficient for the eigenfunction

computation. The *method of snapshots* (Sirovich 1987) is used to solve for the empirical eigenfunctions.

3. Empirical eigenfunctions

As discussed, the K–L procedure will be applied to the hot-wire measurements to identify the organized motions, or coherent structures, in the shear flow. In this regard, the *snapshot form* of the K–L expansion is applied to the free-shear-flow measurements. The calculations of the empirical eigenfunctions for highly resolved flows, such as we have here, present difficulties when approached directly and in fact are not manageable. The *method of snapshots* was developed to solve this problem. A brief discussion of the method which is applied to our experimental data now follows.

3.1. *Construction of the coherent structures via the method of snapshots*

Consider snapshots of the flow field represented by

$$\boldsymbol{v}^{(n)} = \boldsymbol{v}(\boldsymbol{x}, t_n), \tag{6}$$

where $\boldsymbol{v}$ represents the velocity field, which can be expressed by the summation of the time-averaged part, $\overline{\boldsymbol{v}}$, and the fluctuating part, $\boldsymbol{v}'$, i.e.

$$\boldsymbol{v}(\boldsymbol{x}, t) = \overline{\boldsymbol{v}}(\boldsymbol{x}) + \boldsymbol{v}'(\boldsymbol{x}, t). \tag{7}$$

It should be noted that $\boldsymbol{v}$ refers to all velocity components, i.e. here, for our two-dimensional flow, it refers to the streamwise and transverse components. Then we can write the two-point velocity correlations as

$$\boldsymbol{K}(\boldsymbol{x}, \boldsymbol{x}') = \lim_{M \uparrow \infty} \frac{1}{M} \sum_{n=1}^{M} \boldsymbol{v}_n(\boldsymbol{x})\, \boldsymbol{v}_n(\boldsymbol{x}'), \tag{8}$$

where $\boldsymbol{v}_n = \boldsymbol{v}'(\boldsymbol{x}, t_n)$ and the t_n are the uniform sampling times. If the sampling duration is sufficiently large the kernel, $\boldsymbol{K}$, can be approximated by

$$\boldsymbol{K}(\boldsymbol{x}, \boldsymbol{x}') = \frac{1}{M} \sum_{n=1}^{M} \boldsymbol{v}_n(\boldsymbol{x})\, \boldsymbol{v}_n(\boldsymbol{x}'). \tag{9}$$

The kernel, $\boldsymbol{K}$, as represented by (9) is degenerate and as a result has eigenfunctions in the form

$$\boldsymbol{\Psi} = \sum_{k=1}^{M} A_k \boldsymbol{v}_k, \tag{10}$$

where the constants A_k are to be found. By substituting (9) and (10) into the eigenvalue equation, (1), we obtain

$$\boldsymbol{C}\boldsymbol{A} = \lambda \boldsymbol{A}, \tag{11}$$

where

$$\boldsymbol{A} = (A_1, \ldots, A_M) \tag{12}$$

and

$$C_{mn} = \frac{1}{M}(\boldsymbol{v}_m, \boldsymbol{v}_n). \tag{13}$$

In the above, $(\,,)$ is the inner product integrated over the spatial domain of the flow field, i.e.

$$(\boldsymbol{a}, \boldsymbol{b}) = \int_x \int_y a_i\, b_i \, \mathrm{d}x \, \mathrm{d}y. \tag{14}$$

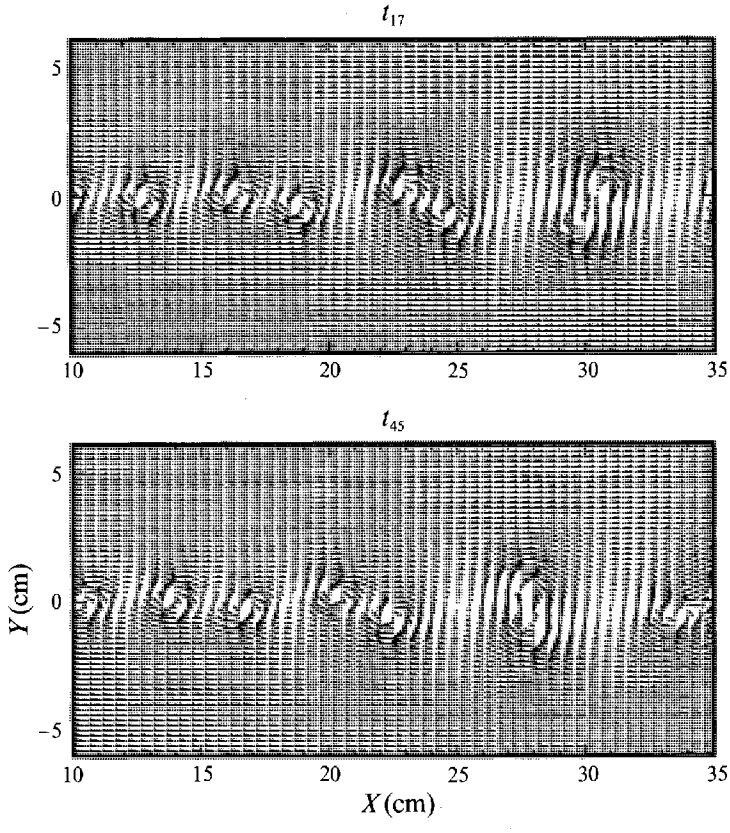

FIGURE 3. Two composite snapshots at t_{17} and t_{45}.

Solution of the matrix eigenvalue problem (11) yields the eigenvalues, λ, representing the energy associated with the modes, and from (10), the eigenfunctions of $\boldsymbol{K}$ which depend on the spatial coordinates only. These fit the boundary conditions of the problem and for incompressible flow also satisfy the continuity equation. We can therefore expand the velocity fluctuations, $\boldsymbol{v}'$, in this set,

$$\boldsymbol{v}'(\boldsymbol{x}, t) = \sum_n a_n(t)\, \boldsymbol{\Psi}_n(\boldsymbol{x}), \tag{15}$$

where the time-dependent coefficients in this expansion, $a_n(t)$, are still to be computed. The N-term finite approximation of the velocity fluctuation is

$$\boldsymbol{v}'_N = \sum_{n=1}^{N} a_n(t)\, \boldsymbol{\Psi}_n(\boldsymbol{x}), \tag{16}$$

truncated at N modes.

3.2. *Application to the experimental data*

Figure 3 shows the velocity vector fields of two composite snapshots at the reference times of t_{17} and t_{45} in the formerly mentioned time frame of the subharmonic component of the driving signal, viewed from a coordinate system moving with one-half the sum of the free-stream velocities. In this time frame $t_{n+1} - t_n = 1/3059$ s. Thus t_{45} represents the flow after one period of the subharmonic instability wave.

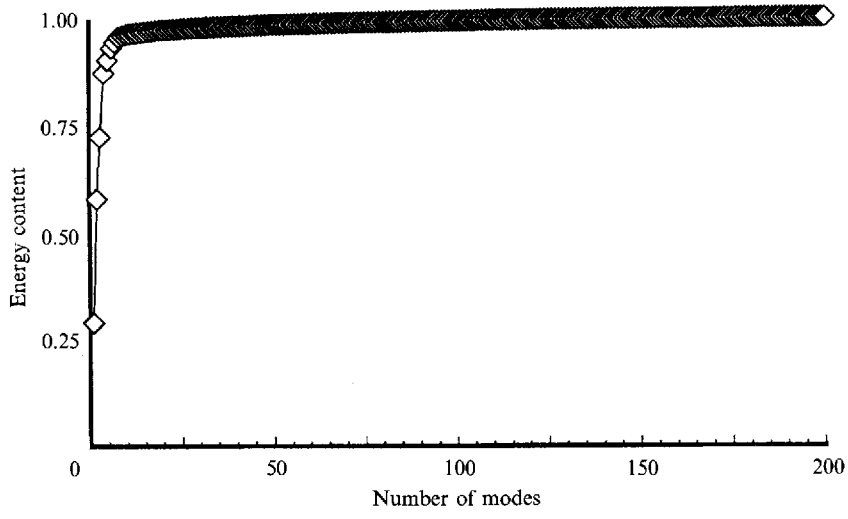

FIGURE 4. The energy content, sum of the eigenvalues, versus the number of modes.

i	λ_i	i	λ_i
1	0.2926	9	0.0031
2	0.2884	10	0.0029
3	0.1502	11	0.00134
4	0.1461	12	0.00131
5	0.0293	13	0.0011
6	0.0288	14	0.00107
7	0.0130	15	0.00105
8	0.0124	16	0.00101

TABLE 1. The first 16 eigenvalues

540 composite snapshots are used to compute the basis set of orthonormal eigenfunctions. This is provided by the solution of a 540×540 matrix eigenvalue problem, equation (11), which produces the eigenvectors. These eigenvectors are then substituted in (10) resulting in 540 eigenfunctions in two components corresponding to the streamwise and transverse components of the velocity field. The energy associated with different eigenfunctions is represented in their corresponding eigenvalue, λ.

Table 1 lists the eigenvalues of the first 16 modes. Figure 4 shows the energy content, summation of eigenvalues, versus the number of eigenmodes in the summation. It is shown that the first four modes contain more than 87% of the fluctuation energy in this flow region. The first eight modes contain more than 96% of the fluctuation energy. The remaining eight modes just contain 1.3% of the fluctuation energy.

To aid in the understanding of the coherent structures associated with the first four eigenfunctions we show these by means of colour graphics. Figure 5 presents the vertical components of the first four eigenfunctions. The dark red regions represent the maximum positive value, upward flow, and the dark blue regions represent the maximum negative value, downward flow. Modes 1 and 2 represent structures associated with the subharmonic instability wave, i.e. the projection of the shear-flow velocity fluctuations on these eigenfunctions has a periodic sine-wave form corresponding to the subharmonic instability wave (figure 6*a*).

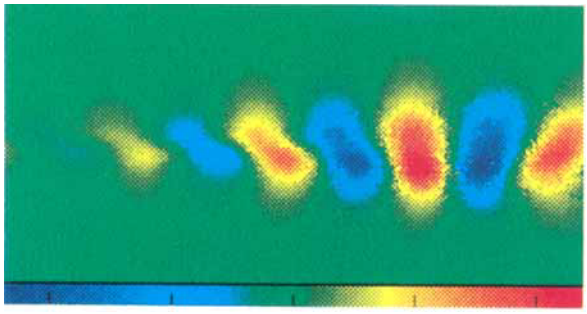

Mode 1

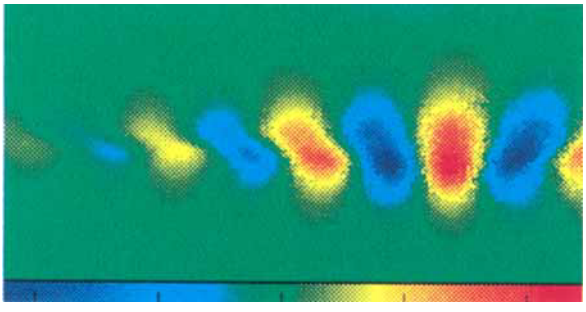

Mode 2

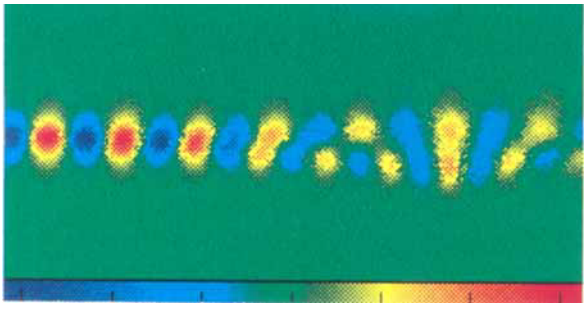

Mode 3

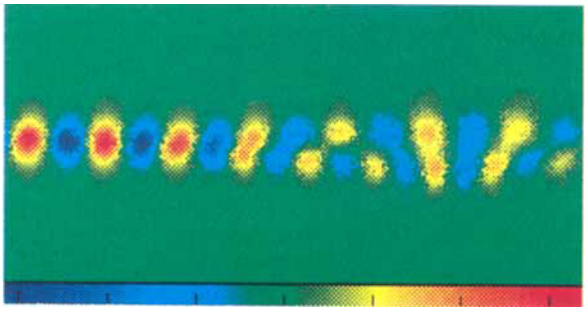

Mode 4

FIGURE 5. The mode 1, 2, 3, and 4 eigenfunctions, vertical component.

The first two empirical eigenfunctions are to a good approximation quarter-wave translates of one another in the streamwise direction. This wavelength shift observed in the eigenmode pairs is the natural outcome of the K–L procedure on the flow and a consequence of near translational invariance in the streamwise direction. The

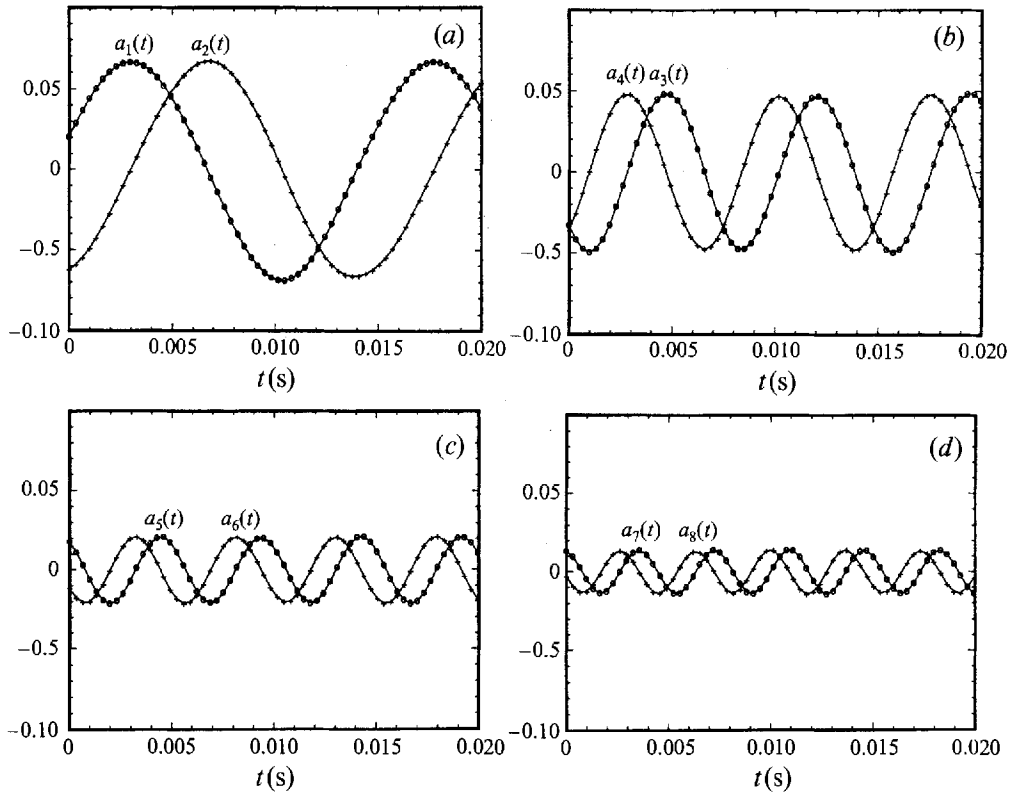

FIGURE 6. Projection of experimental velocity fluctuations on the eigenfunctions of: (*a*) modes 1 and 2, (*b*) modes 3 and 4, (*c*) modes 5 and 6, (*d*) modes 7 and 8.

structures first attain an acute angle with the negative streamwise direction, and with this orientation the work of positive Reynolds stresses of the corresponding disturbance field against the positive rate of strain of the mean flow results in the transfer of energy from the mean flow to the disturbance field of the first two modes. Thus the energy of these two modes reaches its maximum at the streamwise location of the vertical alignment of these structures, i.e. the subharmonic saturation. Note that the contour plots of v (vertical component of the eigenfunction) give an impression of the corresponding stream function ($v \propto \psi$ for a travelling wave) and the net energy production is zero if the v-contours are symmetric in y, which is nearly the case at the location of vertical alignment of the structures, but not elsewhere. However, following their vertical alignment the structures of the first two modes tilt in an acute angle with the positive streamwise direction which in an opposite fashion results in the return of energy from the corresponding disturbance field to the mean flow. The physics of this interaction has been discussed by Mollo-Christensen (1971).

We note in figures 6(*a*) and 5 that mode 1 leads mode 2 by $\frac{1}{2}\pi$ in time but lags it a quarter-wavelength in space. We know that the structures represented by the eigenfunctions are fixed in space. However, when one mode, in the pair, is in the maximum energy state the other is in the minimum energy stage and this relation reverses after one quarter of a period in time. That is, the energy is exchanged between the two modes thereby propagating the flow pattern consisting of the sum of the two in the positive streamwise direction.

Figure 5 also presents the normal components of the second pair of eigenfunctions,

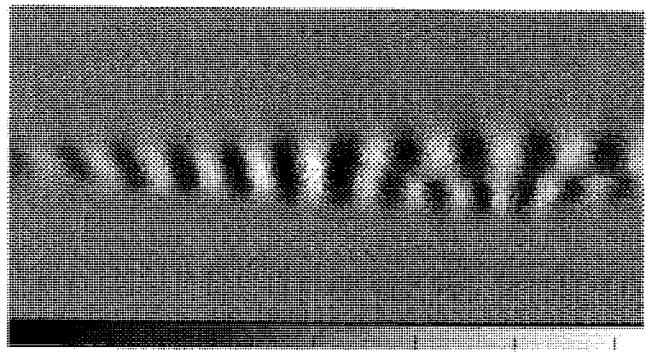

Mode 5

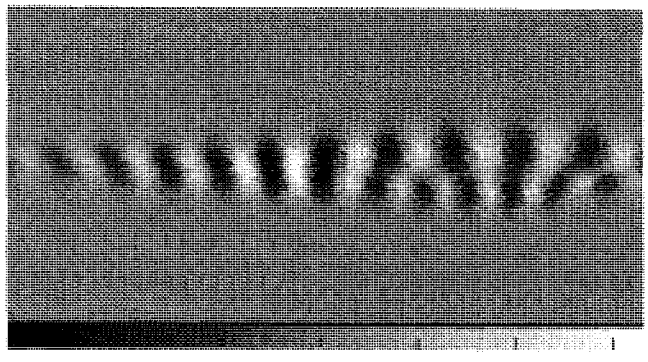

Mode 6

FIGURE 7. The mode 5 and 6 eigenfunctions, vertical component.

modes 3 and 4. These two modes represent the structures associated with the fundamental instability wave, i.e. the projection of the shear-flow velocity fluctuations on these eigenfunctions has a periodic sine-wave form corresponding to the fundamental instability wave (figure 6*b*). We also note that mode 4 leads mode 3 by $\frac{1}{2}\pi$ in time (figure 6*b*) and lags it a quarter-wavelength in space (figure 5), showing quasi-translationally invariant behaviour in the streamwise direction. These modes are already saturated in the upstream flow region under consideration, i.e. 10 to 13 cm downstream of the splitter-plate edge, and lose their energy thereafter.

In the upstream region the structures are vertically aligned where they are in their maximum state of energy. The structures are then tilted at an acute angle with the positive streamwise direction with the result that they lose energy to the mean flow, and split into two smaller structures, one in the high-speed region of the shear flow convecting faster than the other in the lower speed region. This results in two structures with the same frequency but different wavelengths and wave speeds. We refer to this interesting phenomenon as the 'mode degeneration' process which was already indicated in the Fourier space analysis (see Rajaee & Karlsson 1992) and is clearly revealed in these figures. This phenomenon was observed in the field of the fundamental instability wave and its higher harmonics, including the instability waves resulting from the nonlinear interaction of the fundamental instability wave with its first subharmonic and nonlinear interaction of the fundamental instability wave with itself. Therefore, we expect to observe this phenomenon for the structures associated with the eigenfunctions corresponding to the fundamental instability wave and its higher harmonics. That is, we expect similar behaviour from the structures associated

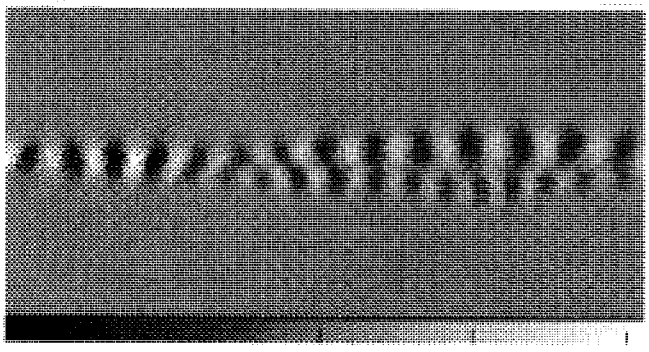

Mode 7

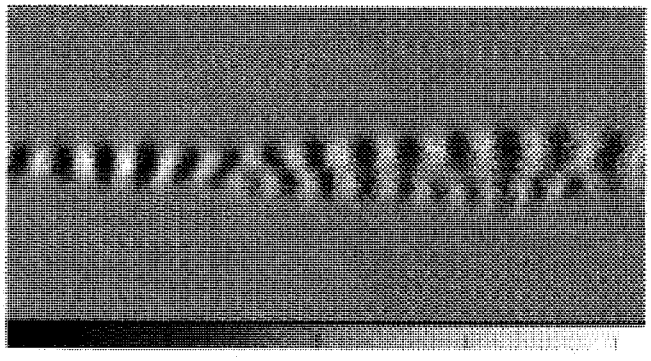

Mode 8

FIGURE 8. The mode 7 and 8 eigenfunctions, vertical component.

with the eigenfunctions of modes 3 and higher. The mode degeneration phenomenon enhances entrainment and mixing.

For the third pair of eigenfunctions, in figure 7, representing three times the subharmonic instability mode, the two wavenumber structures are also observed. The energy of these modes peaks at a location downstream of the maximum energy location of the third and fourth modes before the structures tilt at an acute angle with the positive streamwise direction. Farther downstream the structures evolve to the two wavenumber structures with two wave speeds. Direct projection of velocity fluctuations, from the snapshots, on this pair of eigenfunctions results in two sine waves with the frequency of three times the subharmonic instability wave and a $\frac{1}{2}\pi$ phase difference in time (figure 6*c*). This wave with frequency three times that of the subharmonic instability wave is the result of the nonlinear interaction of subharmonic and fundamental instability waves, thus we can infer that the structures of modes 5 and 6 are the results of nonlinear interactions of the structures of modes 3 and 4 with those of modes 1 and 2. Further study of figure 7 reveals that the location of maximum energy content of modes 5 and 6 is approximately between the maximum energy locations of modes 1, 2 and those of modes 3, 4.

Furthermore, figure 8, representing the normal components of eigenfunctions 7 and 8, corresponding to the first-harmonic instability wave, reveals that the maximum energy locations of modes 7 and 8 coincide with those of modes 3 and 4, clarifying the relation between modes 7, 8 and modes 3, 4. This is because the first-harmonic instability wave, represented by modes 7 and 8, is the result of nonlinear interaction of the fundamental instability wave, represented by the eigenmodes 3 and 4, with itself.

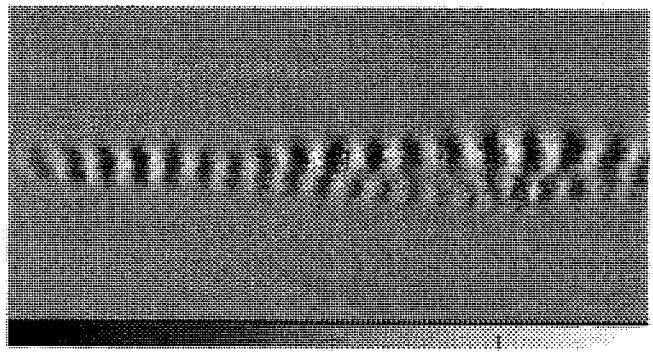

Mode 9

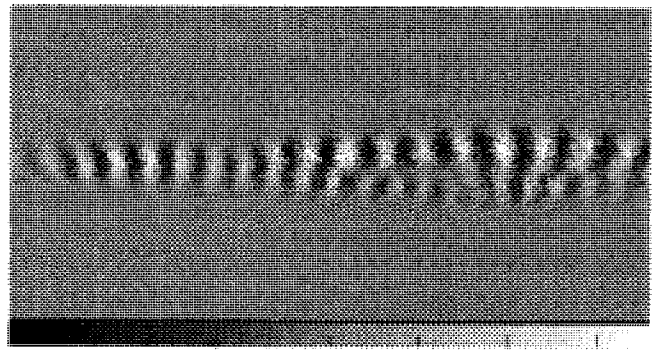

Mode 10

FIGURE 9. The mode 9 and 10 eigenfunctions, vertical component.

The two-wave mode structures of modes 7 and 8 are also observed in figure 8. Figure 6(*d*) shows the result of the projection of velocity fluctuations on this pair of eigenfunctions. Again, the $\frac{1}{2}\pi$ phase difference in time, between the modes, is clearly revealed here.

Figure 9 shows the normal components of the eigenfunctions of modes 9 and 10, which further analysis shows to represent five times the subharmonic instability wave. Even by comparing the number of structures of modes 1 and 2, representing the subharmonic instability wave, with those of modes 9 and 10, one could infer that the structures of modes 9, 10 represent fives times the subharmonic instability wave. From table 1, it is noted that modes 9 and 10 each contain less than 1 % of the energy of the first or the second mode. The modes of number higher than 10, in table 1, each contain about one-third of the energy of mode 10 and, while being insignificant, show regular structures but mostly appear to include the jitter of the regular structures at the frequencies of the subharmonic instability wave and its higher harmonics, as shown by modes 11–13 and 15 in figures 10–12. This claim will be clarified by further spectral analysis of the time-dependent K–L expansion coefficients. By comparing the wavelength of the structures of modes 14 and 16 with those of modes 3 and 4, representing the fundamental instability wave, one finds that they correspond to three times the wavenumber of the fundamental instability wave.

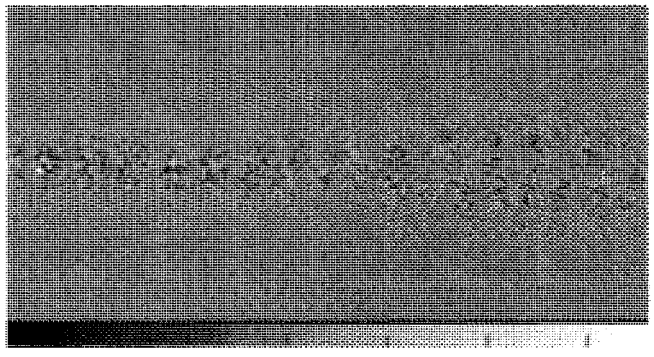

Mode 11

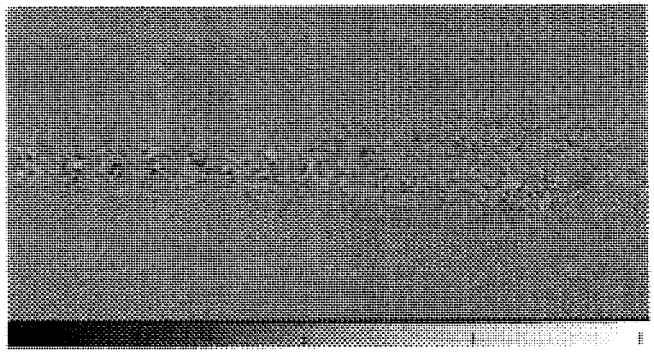

Mode 12

FIGURE 10. The mode 11 and 12 eigenfunctions, vertical component.

4. Dynamics of coherent structures

4.1. *General view*

By studying the dynamics of coherent structures one can attempt to follow the behaviour and evolution of the flow field.

Following the computations of a complete set of vector eigenfunctions, we can approximate the velocity field by its N-term expansion in this set of eigenfunctions, i.e.

$$\boldsymbol{v}(x,y,t) = \bar{\boldsymbol{v}}(x,y) + \sum_{n=1}^{N} a_n(t)\,\boldsymbol{\Psi}_n(x,y), \tag{17}$$

which we substitute into the Navier–Stokes equation, written symbolically as

$$\frac{\partial \boldsymbol{v}}{\partial t} = \boldsymbol{D}(\boldsymbol{v}). \tag{18}$$

The Galerkin approximation to (18), of order N, is obtained by substituting

$$\boldsymbol{v}_N = \bar{\boldsymbol{v}} + \sum_{k=1}^{N} a_k\,\boldsymbol{\Psi}_k \tag{19}$$

into (18) and projecting onto the truncated space,

$$\left(\boldsymbol{\Psi}_k, \left(\frac{\partial \boldsymbol{v}_N}{\partial t} - \boldsymbol{D}(\boldsymbol{v}_N)\right)\right) = 0, \quad k = 1,\ldots,N, \tag{20}$$

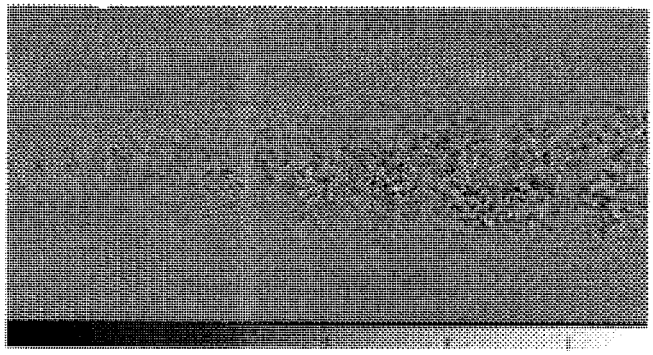

Mode 13

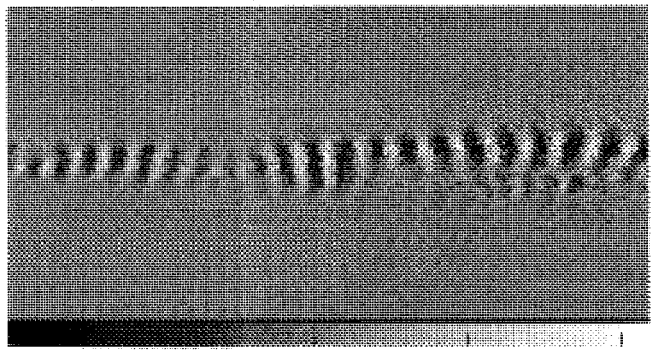

Mode 14

FIGURE 11. The mode 13 and 14 eigenfunctions, vertical component.

and from this

$$\frac{\mathrm{d}a_k}{\mathrm{d}t} = F_k(a_1, \ldots, a_N), \quad k = 1, \ldots, N, \tag{21}$$

where F_k is at most cubic in the coefficients a. This procedure provides a practical procedure for following the turbulent evolution of the flow. In the event of turbulent flow it is necessary to introduce an eddy viscosity to account for the neglected modes (Aubry *et al.* 1988; Zhou & Sirovich (1992).

4.2. *Dynamics of free-shear-flow coherent structures*

The above approach for following the dynamics of coherent structures can be applied to the free-shear flow, but with some fine print. In projecting the Navier–Stokes (N–S) equation along the computed eigenfunctions difficulties are encountered in treating the pressure gradient and because F_k depends functionally on the mean flow, $\bar{v}$. To address these problems we consider the time-averaged N–S equation. Except in the immediate vicinity of the splitter-plate trailing edge, the viscous term in the N–S equation for the shear flow in the wind tunnel is insignificant and neglected,†

$$\frac{\partial \boldsymbol{v}}{\partial t} + \boldsymbol{v} \cdot \nabla \boldsymbol{v} + \nabla p = 0, \tag{22}$$

† Inclusion of the viscous term makes very little change to the solution of the system of dynamical equations. However, it could introduce errors due to the second-order numerical differencing of the empirical eigenfunctions. Figure 13 compares the first-order numerical differencing schemes with the corresponding analytical one, with a grid spacing equivalent to the 1 mm spacing in the experiment, see §4.3.

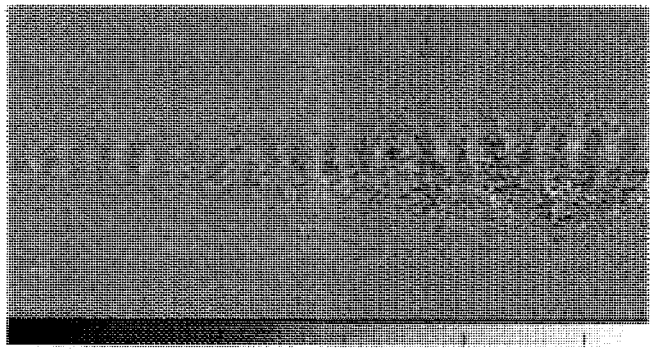

Mode 15

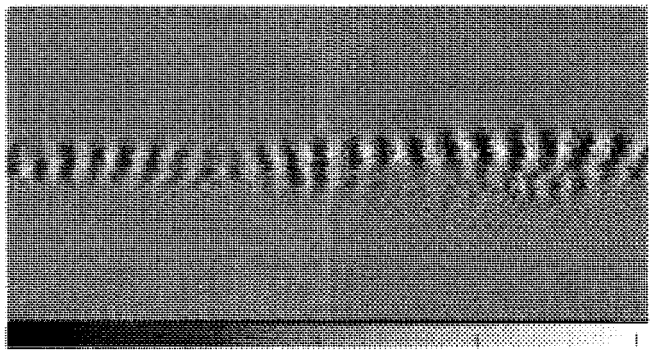

Mode 16

FIGURE 12. The mode 15 and 16 eigenfunctions, vertical component.

where v refers to both mean and fluctuation velocity components, i.e.

$$v = \bar{v} + v'. \tag{23}$$

Substituting (23) in (22) and subtracting the time-averaged (22) from (22) itself results in

$$\frac{\partial v'}{\partial t} + v' \cdot \nabla \bar{v} + \bar{v} \cdot \nabla v' + v' \cdot \nabla v' - \overline{v' \cdot \nabla v'} = -\nabla p', \tag{24}$$

where p' refers to the pressure fluctuation. Substitution of the N-term approximation to the velocity fluctuation, (16), results in

$$\psi_n^i \frac{\mathrm{d}a_n}{\mathrm{d}t} + (\bar{v} \cdot \nabla \psi_n^i + \boldsymbol{\Psi}_n \cdot \nabla \bar{v}^i) a_n + (\boldsymbol{\Psi}_n \cdot \nabla \psi_m^i)[a_n a_m - \overline{a_n a_m}] = -\nabla_i p', \tag{25}$$

with the summation convention on n and m. Next (25) is projected along the eigenfunctions, i.e.

$$\left[\psi_k^i, \left(\psi_n^i \frac{\mathrm{d}a_n}{\mathrm{d}t} + (\bar{v} \cdot \nabla \psi_n^i + \boldsymbol{\Psi}_n \cdot \nabla \bar{v}^i) a_n + (\boldsymbol{\Psi}_n \cdot \nabla \psi_m^i)[a_n a_m - \overline{a_n a_m}] = -\nabla_i p'\right)\right], \tag{26}$$

with the summation convention on i, n and m. Equation (26) can be put in the form

$$\frac{\mathrm{d}a_k}{\mathrm{d}t} + B^{kn} a_n + C^{knm}(a_n a_m - \overline{a_n a_m}) = D^k, \tag{27}$$

where
$$B^{kn} = (\psi_k^i, (\bar{v}\cdot\nabla\psi_n^i + \boldsymbol{\Psi}_n\cdot\nabla\bar{v}^i)), \tag{28}$$

and for the moment we regard $\bar{v}$ as a known function. Also

$$C^{knm} = (\psi_k^i, (\boldsymbol{\Psi}_n\cdot\nabla\psi_m^i)), \tag{29}$$

and
$$D^k = (\psi_k^i, (-\nabla_i p')). \tag{30}$$

Using the divergence theorem and the fact that each of the eigenfunctions satisfies the continuity, we obtain

$$\begin{aligned} D^k &= -\iint \psi_k^i \nabla_i p' \,\mathrm{d}x\,\mathrm{d}y \\ &= -\iint (\nabla\cdot(p'\,\boldsymbol{\Psi}_k) - p'(\nabla\cdot\boldsymbol{\Psi}_k))\,\mathrm{d}x\,\mathrm{d}y \\ &= -\oint n^i \psi_k^i p' \,\mathrm{d}s, \end{aligned} \tag{31}$$

so that D^k depends only on the flow at the boundaries. In the following we will take

$$D^k \approx 0.$$

This obtains if for example $\boldsymbol{n}\cdot\boldsymbol{\Psi}_k = 0$ on the boundaries or if the pressure fluctuation vanishes there, or some combination of these occurs.

Consequently the system of dynamical equations we consider is given by

$$\frac{\mathrm{d}a_k}{\mathrm{d}t} + B^{kn}a_n + C^{knm}(a_n a_m - \delta_{nm}\overline{a_n^2}) = 0, \tag{32}$$

using the fact that the modes are uncorrelated, i.e. $\overline{a_n a_m} = \delta_{nm}\overline{a_n^2}$, where δ_{nm} is the Kronecker delta. With the solution of this system of dynamical equations, the dynamics of coherent structures can be studied which, with further analytical work, results in a procedure for following the turbulent evolution of the shear flow.

4.3. *Solution of the system of dynamical equations*

The computed eigenfunctions are used to obtain the constant coefficients of the dynamical equations, i.e. B^{kn} and C^{knm}, from (28) and (29). The first sixteen modes, each with energy percentage $\geqslant 0.1\,\%$ of the total two-dimensional fluctuation energy, are considered for the system of dynamical equations to include all the significant harmonics of the subharmonic instability wave. A system of sixteen equations with sixteen unknowns is solved, (32), using the experimental initial condition for the $a_n(t=0)$, i.e. from the direct projection of the first snapshot, at $t=0$, on the eigenfunctions. The fourth-order Runge–Kutta scheme, for the explicit integration, is used with the running-time-average $\overline{a_n^2}$ term. The code is tested for numerical dissipation with different time steps and is seen not to be a dissipative scheme. The time step used in this simulation is the same as the time interval between the experiment snapshots so that the experimental $a_n(t)$ from direct projection of snapshots on the eigenfunctions can be compared to the simulation results, from (32).

The experiment was performed with a relatively dense grid spacing in order to improve the accuracy of the spatial differencing scheme, but it is difficult to eliminate differencing errors. A two-point differencing scheme is used for the boundary locations, a three-point scheme for the immediate neighbouring nodes of the boundary nodes and

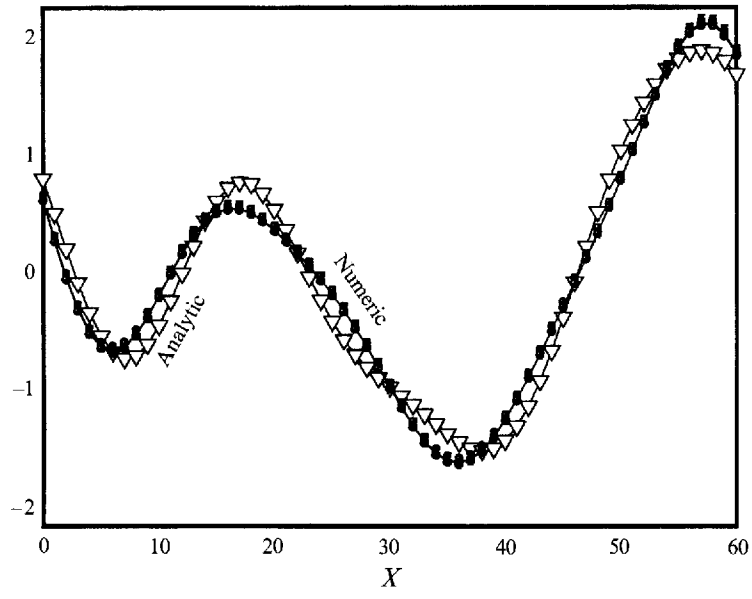

FIGURE 13. Comparing three-, four- and five-point differencing schemes with the corresponding analytical differencing.

a five-point scheme for all the other grid nodes in the flow region (see the Appendix). In order to have a feeling for the accuracy of the numerical differencing scheme a numerical test was done. An analytical signal composed of four sine-waves with the wavenumbers of the subharmonic instability wave and its three higher harmonics is chosen, approximately simulating the first four pairs of eigenfunctions with amplitude ratios proportional to their eigenvalues and with arbitrary phase differences. The grid spacing in this simulation is equivalent to that of the shear-flow experiment. Figure 13 compares the analytical differencing result with those of the three-, four- and five-point numerical differencing schemes. The results from three-, four- and five-point differencing schemes are close and cannot be distinguished in the plot. It is quite revealing that there is some error. This error could result in some inaccuracy in the solution of the system of dynamical equations.

The computed $a_n(t)$ are compared to the direct projection results in figure 14(*a–d*) for the first 16 modes. There is a second frequency, a low-frequency modulation, observed in the simulation results which could be due to error in computing the constant coefficients of the dynamical equations, i.e. B^{kn} and C^{knm}. This is the consequence of the error in the numerical differencing scheme. Also, since the mean flow velocity is a time average, or ensemble average over the number of snapshots, i.e. 540 snapshots taken in less than 0.2 s, it could be possible that the mean flow estimate for the small transverse component includes some inaccuracy which could in turn cause an error in B^{kn}.

Figure 14(*a–d*) shows that the simulation solid lines, obtained by solving the system of dynamical equations compare reasonably well with the direct projections of snapshots on the eigenfunctions, the dotted lines. For the first pair of most energetic modes in particular, with the sum of more than 58% of the fluctuation energy, the results from the dynamical equations are close to the direct projection results. The presence of a low-frequency modulation is more obvious in the results of higher-frequency modes, specially the second pair of modes. The frequency response of the

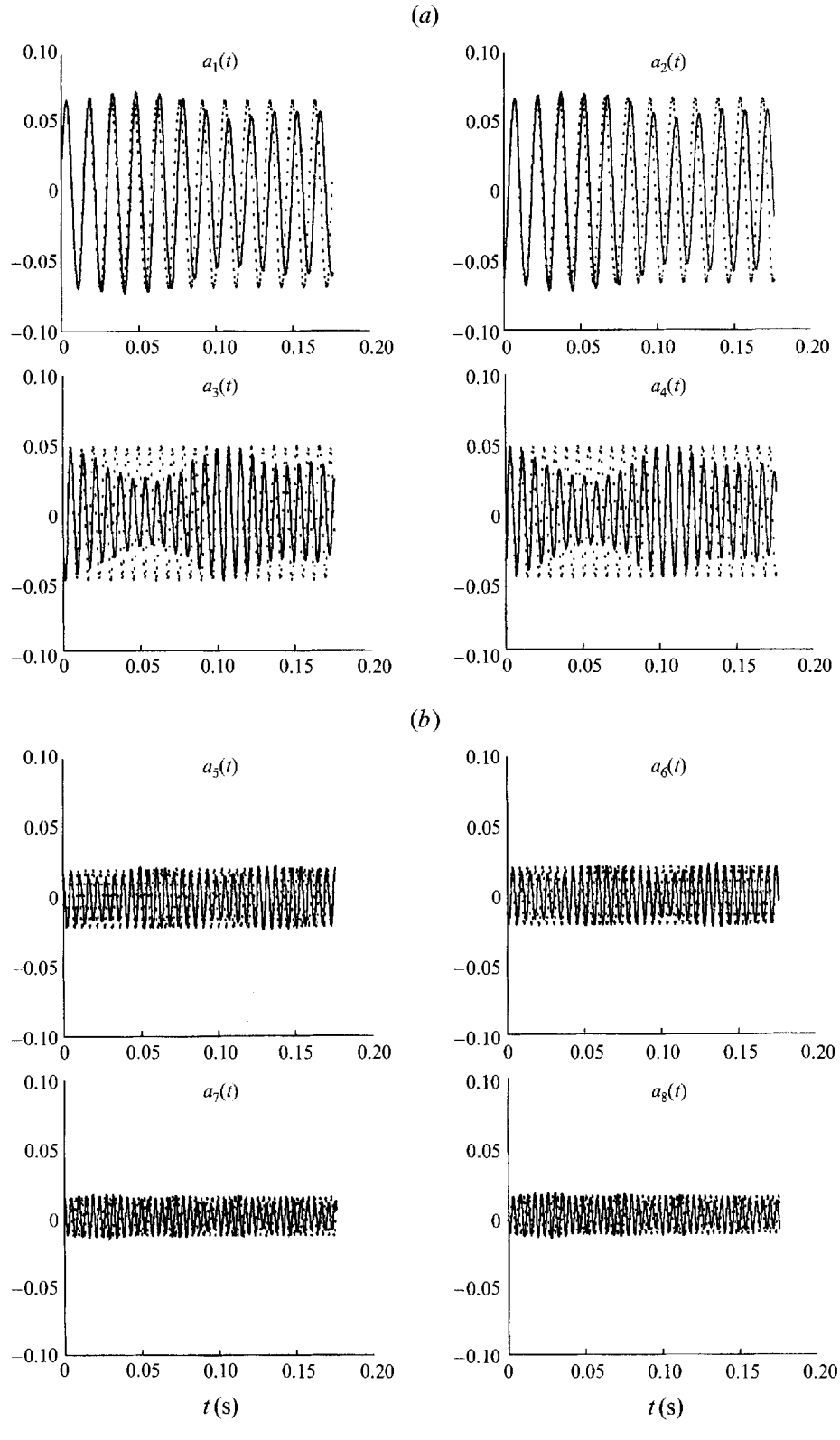

FIGURE 14(*a*, *b*). For caption see facing page.

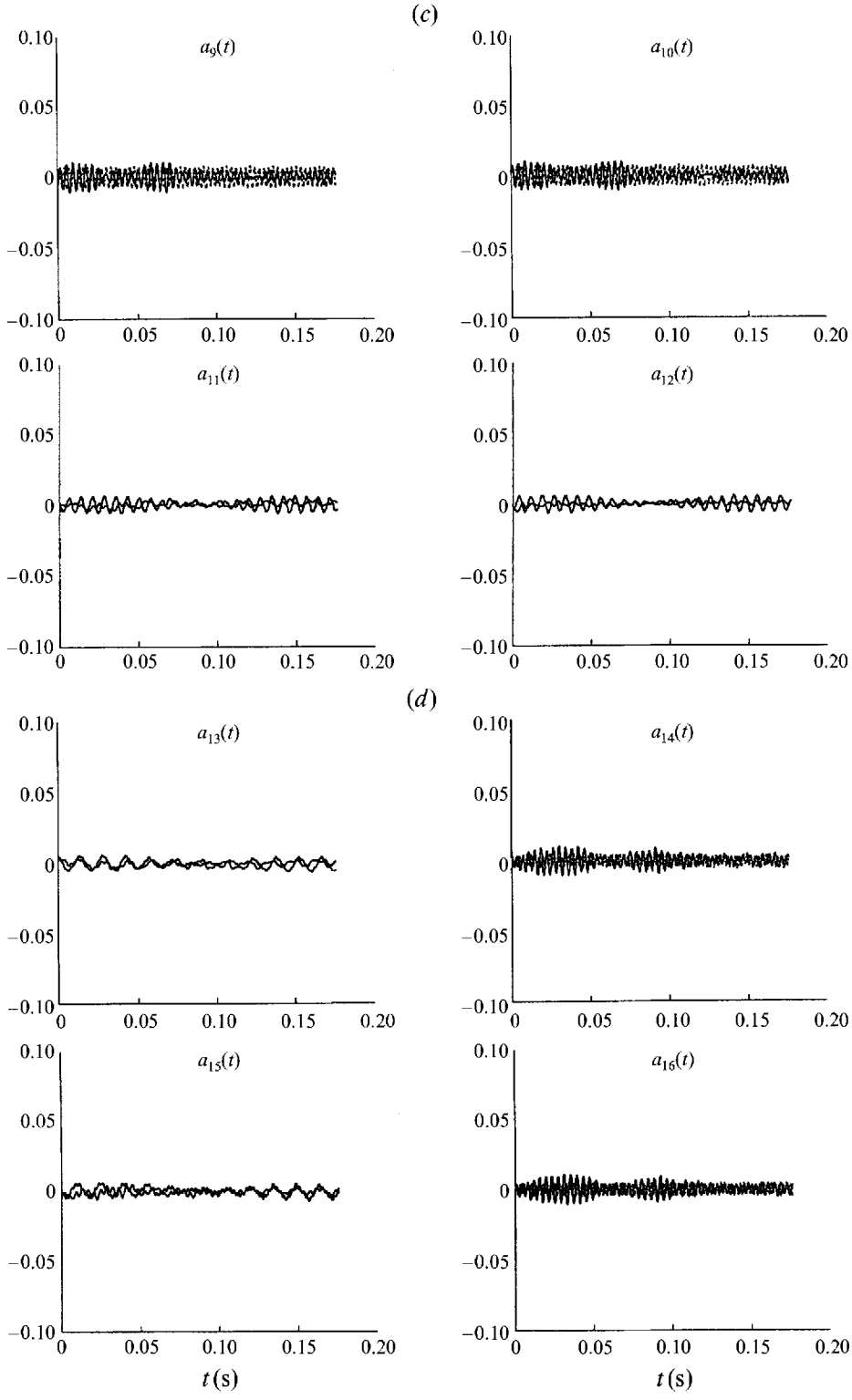

FIGURE 14. (*a*) $a_1(t) \cdots a_4(t)$, from direct projection of snapshots on the eigenfunctions (dotted line), and computed from dynamical equations (solid line); (*b*) $a_5(t) \cdots a_8(t)$; (*c*) $a_9(t) \cdots a_{12}(t)$; (*d*) $a_{13}(t) \cdots a_{16}(t)$. In each case *all* 16 *modes are considered.*

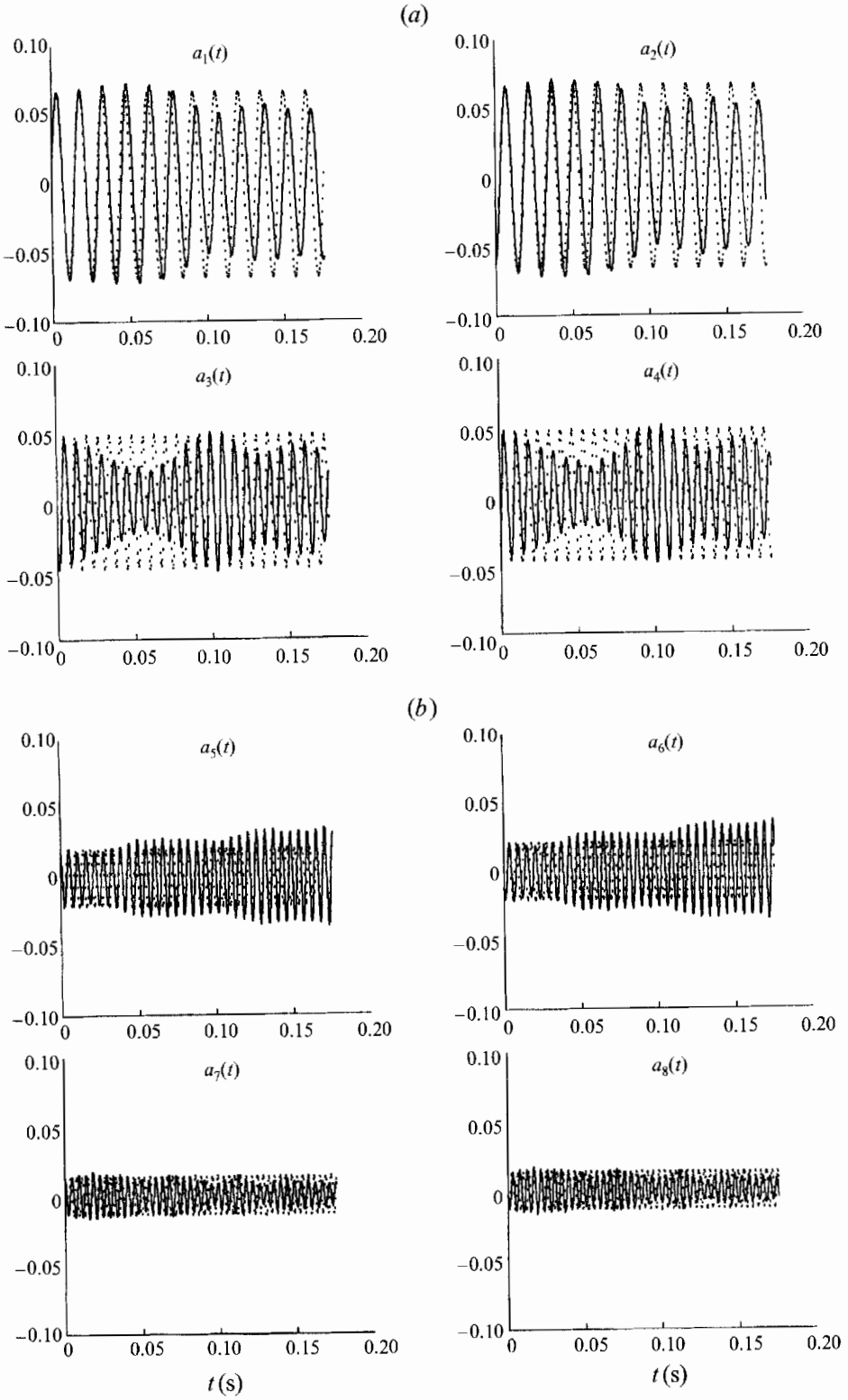

FIGURE 15. (*a*) $a_1(t) \cdots a_4(t)$, from direct projection of snapshots on the eigenfunctions (dotted line), computed from dynamical equations (solid line); (*b*) $a_5(t) \cdots a_8(t)$, *considering* 8 *modes.*

solution is not exactly the same as the one from the direct projection of snapshots on the eigenfunctions. The error in the frequency response is caused by the error in the constant coefficients of the dynamical equations, mostly because of the error in B^{kn} which could be a consequence of the numerical differencing error in computing the derivatives of the mean flow and the eigenfunctions.

From table 1 it is noted that the first eight modes contain more than 96% of the fluctuation energy while the next eight modes contain only 1.3% of the energy. Thus, it would seem that if only the first eight modes are considered the results should be almost the same as the case of sixteen modes. However, as figure 15(*a*, *b*) shows, there are some differences between the results from considering eight modes in the system of dynamical equations and the ones from sixteen modes (figure 14) which appear mostly in modes 5 and 6. It appears that the second eight modes, 9–16, while not being that significant from an energy content point of view, are dynamically more active than their eigenvalues suggest because they include higher-frequency disturbances. As later spectral plots will show, the second eight modes not only contain higher harmonics of fundamental and subharmonic modes, such as five times the subharmonic and six times the subharmonic instability waves, but also contain contributions at the subharmonic frequency and its three higher harmonics. Therefore, when only the first eight modes are considered in the system of dynamical equations, there is only a slight affect in the solutions for the first four modes corresponding to the subharmonic and fundamental instability waves, but there is a dominant growing effect in the fifth and sixth modes, figure 15(*b*). Apparently, when considered in this way, a part of the mean flow energy which could be transferred to the second eight modes is fed to the fifth and sixth modes. The following discussion will reveal that most of the fluctuation energy at the frequencies of the subharmonic and its significant higher harmonics, including jitter, will be included by considering the first sixteen modes in the system of dynamical equations.

The spectral analysis of the experimental $a_n(t)$ values is shown in figure 16(*a–d*), and it should be noted that the scale is logarithmic. It reveals that each pair of neighbouring modes of almost equal energy, or eigenvalues, represents one hydrodynamic instability wave, i.e. the first pair including modes 1 and 2 represents the subharmonic, the second pair including the third and fourth modes represents the fundamental and the other pairs represent higher harmonics of the subharmonic. This is true for the first five pairs. The spectral analysis of modes 11, 12 from the sixth pair, figure 16(*c*), shows that the time-dependent K–L expansion coefficients, corresponding to these eigenfunctions, have dominantly the frequency of the fundamental instability wave. The corresponding eigenfunctions, figure 10, with the eigenvalues each representing about 0.1% of the energy of the total fluctuation energy, show, although somewhat diffusely, structures with the wavelengths of modes 3 and 4. This weak energy structure apparently shows the contribution of the phase jitter of the fundamental instability wave occurring with a frequency equal to six times the subharmonic, which cannot be represented by modes 3 and 4. The eigenfunction plots of modes 13–16 (figures 11 and 12) together with figures 14(*d*) and 16(*d*) reveal that modes 14 and 16 mostly represent structures associated with six times the subharmonic instability wave. They also show that the structures associated with modes 13 and 15 contain relatively greater contributions from the subharmonic instability wave, which may represent the phase jitter of this wave at a frequency equal to six times the subharmonic, which cannot be represented by modes 1 and 2.

The frequency response of the solution of the system of dynamical equations for the first eight higher energy modes are close to the corresponding direct projection of

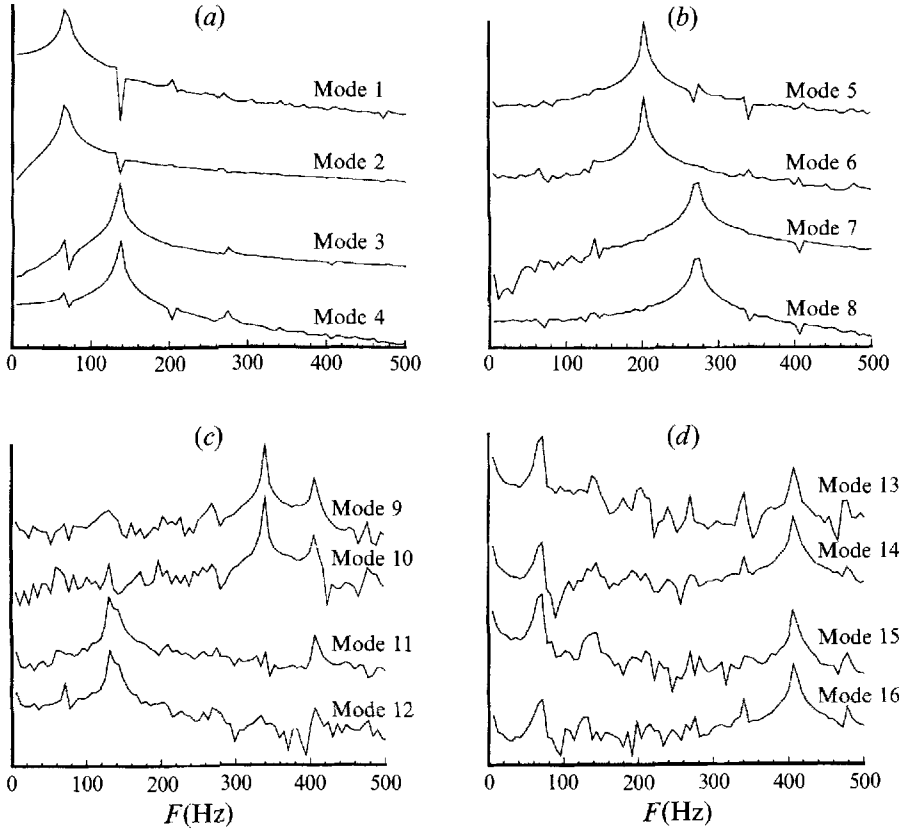

FIGURE 16. Spectrum of (*a*) $a_1(t) \cdots a_4(t)$, (*b*) $a_5(t) \cdots a_8(t)$, (*c*) $a_9(t) \cdots a_{12}(t)$, (*d*) $a_{13}(t) \cdots a_{16}(t)$; direct projection results.

snapshots on the eigenfunctions. Even for the very low energy mode 9 and consecutive modes the solution of the system of dynamical equations are close to the direct projection results while the frequency response might not be satisfactory. In general the results are very encouraging despite the experimental constraints such as numerical differencing of the eigenfunctions and mean flow velocity as well as lack of experimental information regarding the pressure fluctuations at the right and left boundaries of the flow region. As discussed earlier, the slight error in the frequency response of the solution could be due to the error in the constant coefficients of the system of dynamical equations which are computed despite having the disadvantage of the formerly mentioned experimental constraints. However, the simulation results well describe the dynamical behaviour of the shear flow coherent structures associated with the principal eigenfunctions.

4.4. *Mean flow simulation*

Next we address the question of determining the mean flow. The time averaged Navier–Stokes equations are given by

$$\left.\begin{aligned} \nabla \cdot U &= 0, \\ U_j \frac{\partial U_i}{\partial x_j} + \frac{\partial}{\partial x_j}(\overline{u_i u_j}) + \frac{\partial P}{\partial x_i} &= 0, \end{aligned}\right\} \tag{33}$$

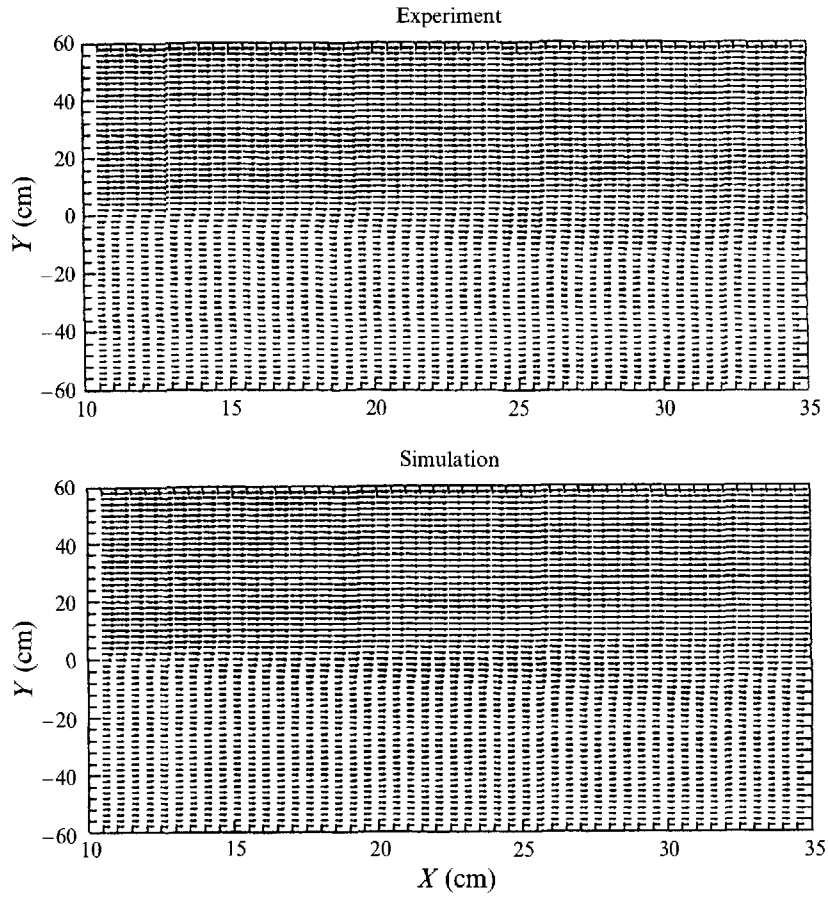

FIGURE 17. Velocity vector field of the mean flow, comparing the results of simulation with the experiment, where the mean pressure gradient is computed from the Navier–Stokes equations and used in the mean flow simulation.

where the dissipation term is neglected because it is insignificant for this flow. The Reynolds stress term $(\partial/\partial x_j)(\overline{u_i u_j})$ can be computed from the computed set of empirical eigenfunctions and the simulation results of the system of dynamical equations, namely

$$\begin{aligned}\overline{u_i u_j}(x,y) &= \sum \overline{a_n(t)\,\psi_i^n(x,y)\,a_m(t)\,\psi_j^m(x,y)} \\ &= \sum \psi_i^n(x,y)\,\psi_j^m(x,y)\,\overline{a_n(t)\,a_m(t)} \\ &= \sum \overline{a_n^2}\,\psi_i^n(x,y)\,\psi_j^n(x,y), \end{aligned} \tag{34}$$

where $\psi_i^n(x,y)$ and $\psi_j^n(x,y)$ represent the eigenfunctions and $a_n(t)$ represents the time-dependent K–L expansion coefficients computed from the system of dynamical equations. In arriving at the final form of (34) we have used $\overline{a_n a_m} = 0$, $m \neq n$.

From the mathematical point of view the solution of system (33) is straightforward, if $\boldsymbol{U}\cdot\boldsymbol{n}$ is known on the boundaries of the domain. We assume that this is the case. In this sense we model the actual experimental situation. We take $\boldsymbol{U}\cdot\boldsymbol{n} = 0$ on the horizontal walls and $\boldsymbol{U}\cdot\boldsymbol{n}$ given at the up and downstream vertical boundaries. (This is consistent with our earlier assumption that $\boldsymbol{\Psi}\cdot\boldsymbol{n} = 0$ on boundaries.) The hope is that this will be a good enough model of the actual situation.

Equation (33) can be written for the streamwise and transverse directions in the following form:

$$U_1 \frac{\partial}{\partial x} U_1 + U_2 \frac{\partial}{\partial y} U_1 = f(x, y), \tag{35}$$

$$U_1 \frac{\partial}{\partial x} U_2 + U_2 \frac{\partial}{\partial y} U_2 = g(x, y), \tag{36}$$

where $f(x, y)$ and $g(x, y)$ include the Reynolds stress and the mean pressure gradient terms. The subscripts 1 and 2 refer to the streamwise and transverse directions, respectively. Assuming that the pressure term is known, (35) and (36) can be solved by the method of characteristics. Thus

$$\frac{\mathrm{d}x}{U_1} = \frac{\mathrm{d}y}{U_2} = \frac{\mathrm{d}U_1}{f} = \frac{\mathrm{d}U_2}{g}. \tag{37}$$

Equation (37) is in fact three equations, one of which gives the equation for the characteristics lines, (38), while the other two, (39), provide the solutions for the mean flow velocity components on the characteristics lines, i.e.

$$\frac{\mathrm{d}y}{\mathrm{d}x} = \frac{U_2}{U_1}, \tag{38}$$

and

$$\frac{\mathrm{d}U_1}{\mathrm{d}x} = \frac{f}{U_1}, \quad \frac{\mathrm{d}U_2}{\mathrm{d}x} = \frac{g}{U_1}. \tag{39}$$

Equation (38) shows that the characteristics lines are in fact the mean flow streamlines. To solve (38) and (39) for the experiment with the equidistance grid nodes, it is convenient to advance in the streamwise direction one grid spacing step and compute for the transverse profile of the velocity field at that fixed streamwise location. However, the streamlines do not necessarily pass the equidistance grid nodes, therefore one has to interpolate for the velocity field at the equidistance nodes in the transverse direction and proceed for the next step in the streamwise direction.

4.5. *Mean flow computations*

A successful solution of the system of dynamical equations raises the hope that one might reconstruct the mean flow field from the simulated Reynolds stresses through the eigenfunctions and the $a_n(t)$ from the dynamical equations, and then by changing some flow parameter, e.g. Reynolds number, be able to predict flow variation.

In order to check the accuracy of the numerical scheme for the mean flow computations by the *method of characteristics*, the mean pressure gradient is first computed from the Navier–Stokes equations, using the experimental velocity measurements, and used in the right-hand sides of (39), i.e. f and g. The result is very close to the experimental mean flow. Figure 17 compares the mean flow simulation to the corresponding experimental result. Therefore, the numerical scheme, based on the method of characteristics, is shown to work. However, the problem of the lack of a mean pressure term remains to be solved.

5. Summary and conclusions

It is found that most of the fluctuation energy is carried by the first few modes in the empirical eigenfunction space obtained from the K–L expansion procedure. Therefore, a low-dimensional eigenfunction space is obtained which describes the shear-flow

coherent structures. Even the phase jitter associated with these large-scale structures can be captured by a few low-energy modes. Among the first few pairs of modes, each pair represents one hydrodynamic instability wave, one mode leading its companion in the pair by a quarter-wavelength in space, i.e. showing the characteristics of a translationally quasi-invariant flow, and lagging it a quarter-period in time.

Projection of the Navier–Stokes equations on this basis set of principal eigenfunction modes results in a low-order system of dynamical equations. Solution of this system of equations describes the dynamics of the coherent structures associated with these eigenfunctions. The simulation, as obtained from the system of dynamical equations, compares well with the direct projections of the snapshots on the eigenfunctions. This is very encouraging. The successful solution of the system of dynamical equations as well as the preliminary mean flow simulation, although not quite successful due to the lack of mean pressure gradient, are promising indications of being able to use the computed set of principal eigenfunctions from the experiment and numerically, by changing some flow parameter, e.g. Reynolds number, follow the evolution of the shear flow. If Reynolds number $\boldsymbol{R} \neq \boldsymbol{R}_0$ the set of eigenfunctions, $\{\Psi_n^0\}$, calculated for $\boldsymbol{R}_0$, are no longer, in general, the coherent structures of the flow. However, $\{\Psi_n^0\}$ still form a complete orthonormal set satisfying the continuity equation. The calculated set $\{\Psi_n^0\}$ might therefore be expected to be useful over a range of parameter space, $\boldsymbol{R}$, or could be used to form a new basis set of eigenfunctions, $\{\Psi_n\}$, for a flow with a different Reynolds number.

This work was supported by DARPA under ONR N00014-86-K0754.

Appendix. The differencing scheme

Both sets of coefficients, B^{kn} and C^{knm}, in the system of dynamical equations (32) involve spacial numerical differencing in the (X, Y)-plane, and there are 251×121 grid points in the (X, Y)-plane flow region. We take $\mathrm{d}x$ and $\mathrm{d}y$ to be the spacial grid spacing in the X- and Y-directions, respectively. In the experiment $\mathrm{d}x = \mathrm{d}y = 1$ mm.

The spatial numerical differencing at the inner grid points is based on the five-point differencing scheme, i.e.

$$\left.\begin{aligned} \left.\frac{\partial U}{\partial x}\right|_{(ix,iy)} &= (-2U_{(ix+2,iy)} + 2U_{(ix-2,iy)} + 16U_{(ix+1,iy)} - 16U_{(ix-1,iy)})/24\,\mathrm{d}x \\ \left.\frac{\partial U}{\partial y}\right|_{(ix,iy)} &= (-2U_{(ix,iy+2)} + 2U_{(ix,iy-2)} + 16U_{(ix,iy+1)} - 16U_{(ix,iy-1)})/24\,\mathrm{d}y. \end{aligned}\right\} \quad \text{(A 1)}$$

The numerical differencing along the border grid points with the tangential gradient direction, except the four corners and the grid points next to them, is also based on the above-mentioned five-point scheme.

The differencing at the border grid points with the normal gradient direction, as well as at the four corners of the flow region, is simply based on the two-point differencing scheme, i.e.

$$\left.\begin{aligned} \left.\frac{\partial U}{\partial x}\right|_{(1,iy)} &= (U_{(2,iy)} - U_{(1,iy)}/\mathrm{d}x, \qquad \left.\frac{\partial U}{\partial x}\right|_{(NX,iy)} = (U_{(NX,iy)} - U_{(NX-1,iy)})/\mathrm{d}x \\ \left.\frac{\partial U}{\partial y}\right|_{(ix,1)} &= (U_{(ix,2)} - U_{(ix,1)})/\mathrm{d}y, \quad \left.\frac{\partial U}{\partial y}\right|_{(ix,NY)} = (U_{(ix,NY)} - U_{(ix,NY-1)})/\mathrm{d}y. \end{aligned}\right\} \quad \text{(A 2)}$$

A three-point differencing scheme is used for the grid points next to the border grid points, with the normal gradient direction:

$$\left.\begin{aligned} \left.\frac{\partial U}{\partial x}\right|_{(2,iy)} &= (U_{(3,iy)} - U_{(1,iy)})/2\mathrm{d}x, \quad \left.\frac{\partial U}{\partial x}\right|_{(NX-1,iy)} = (U_{(NX,iy)} - U_{(NX-2,iy)})/2\,\mathrm{d}x, \\ \left.\frac{\partial U}{\partial y}\right|_{(ix,2)} &= (U_{(ix,3)} - U_{(ix,1)})/2\,\mathrm{d}y, \quad \left.\frac{\partial U}{\partial y}\right|_{(ix,NY-1)} = (U_{(ix,NY)} - U_{(ix,NY-2)})/2\,\mathrm{d}y. \end{aligned}\right\} \tag{A 3}$$

REFERENCES

AHMED, N. & GOLDSTEIN, M. H. 1975 *Orthogonal Transforms for Digital Signal Processing.* Springer.

ASH, R. B. & GARDNER, M. F. 1975 *Topics in Stochastic Processes.* Academic.

AUBRY, N., HOLMES, P., LUMLEY, J. L. & STONE, E. 1988 The dynamics of coherent structures in the wall region of a turbulent boundary layer. *J. Fluid Mech.* **192**, 115.

BAKEWELL, P. & LUMLEY, J. L. 1967 Viscous sublayer and adjacent wall region in turbulent pipe flow. *Phys. Fluids* **10**, 1880.

BROWAND, F. K. & WEIDMAN, P. D. 1976 Large scales in the developing mixing layer. *J. Fluid Mech.* **76**, 127.

BROWN, G. L. & ROSHKO, A. 1974 On density effects and large structure in turbulent mixing layers. *J. Fluid Mech.* **64**, 775.

DIMOTAKIS, P. & BROWN, G. 1976 The mixing layer at high Reynolds number: large-structure dynamics and entrainment. *J. Fluid Mech.* **78**, 535.

FUKUNAGA, K. 1972 *Introduction to Statistical Pattern Recognition.* Academic.

FUKUOKA, A. A. 1951 A study on 10-day forecast (A synthetic report). *Geophys. Mag.* **177**.

GLAUSER, A., LIEB, S. J. & GEORGE, N. K. 1987 Coherent structures in the axisymmetric turbulent jet mixing layer. In *Turbulent Shear Flows 5* (ed. F. Durst, B. E. Launder, J. L. Lumley *et al.*), p. 134. Springer.

GLEZER, A., KADIOGLU, Z. & PEARLSTEIN, A. J. 1989 Development of an extended proper orthogonal decomposition and its application to a time periodically forced plane mixing layer. *Phys. Fluids* A **1**, 1363.

HERZOG, S. 1986 The large scale structures in the near wall region of turbulent pipe flow. PhD thesis, Cornell University.

HO, C.-M. & HUANG, L. S. 1982 Subharmonics and vortex merging in mixing layers. *J. Fluid Mech.* **119**, 443.

HO, C.-M. & HUERRE, P. 1984 Perturbed free shear layers. *Ann. Rev. Fluid Mech.* **16**, 365.

HUANG, L. S. & HO, C.-M. 1990 Small-scale transition in a plane mixing layer. *J. Fluid Mech.* **210**, 475.

KAWAKUBO, T. 1990 Characteristic-eddy decomposition of turbulent mixing layer. *Proc. 17th Intl Symp. on Space Technology and Science*, p. 2337. Tokyo: Japan Publications Trading Co.

KUTZBACH, J. E. 1967 Empirical eigenvectors of sea-level pressure, surface temperature and precipitation complexes over North America. *J. Appl. Met.* **6**, 791.

LOÈVE, M. 1955 *Probability Theory*, Van Nostrand.

LORENZ, E. N. 1956 Empirical orthogonal functions and statistical weather prediction. *Sci. Rep.* No. 1, Statistical Forecasting Project, Department of Metrology, MIT.

LUMLEY, J. L. 1967 The structure of inhomogeneous turbulent flows. In *Atmospheric Turbulence and Radio Wave Propagation* (ed. A. M. Yaglom & V. I. Tatarski), p. 166. Moscow: Nauka.

LUMLEY, J. L. 1981 Coherent structures in turbulence. In *Transition and Turbulence* (ed. R. E. Meyer), p. 215. Academic.

MICHALKE, A. & HERMANN, J. 1982 On the inviscid instability of a circular jet with external flow. *J. Fluid Mech.* **114**, 343.

MOIN, P. 1984 Probing turbulence via large eddy simulation, *AIAA 22nd Aerospace Sciences Meeting.*

MOLLO-CHRISTENSEN, E. 1971 Physics of turbulent flow. *AIAA J.* **9**, 1217.

MONKEWITZ, P. A. & HUERRE, P. 1982 Influence of the velocity ratio on the spatial instability of mixing layers. *Phys. Fluids* **25**, 1137.

PAYNE, F. R. & LUMLEY, J. L. 1967 Large eddy structure of the turbulent wake behind a circular cylinder. *Phys. Fluids* **10**, S194.

PREISENDOFER, R. 1988 *Principal Component Analysis in Meteorology and Oceanography.* Elsevier.

RAJAEE, M. 1991 Measurement and mathematical analysis of free shear flow. PhD thesis, Brown University.

RAJAEE, M. & KARLSSON, S. K. F. 1990 Shear flow coherent structures via Karhunen–Loève expansion. *Phys. Fluids* A **2**, 2249.

RAJAEE, M. & KARLSSON, S. K. F. 1992 On the Fourier space decomposition of free shear flow measurements and mode degeneration in the pairing process. *Phys. Fluids* A **4**, 321.

SIROVICH, L. 1987*a* Turbulence and the dynamics of coherent structures, Part 1: Coherent structures. *Q. Appl. Maths* **45/3**, 561.

SIROVICH, L. 1987*b* Turbulence and the dynamics of coherent structures, Part 2: Symmetries and transformations. *Q. Appl. Maths* **45/3**, 573.

SIROVICH, L. 1987*c* Turbulence and the dynamics of coherent structures, Part 3: Dynamics and scaling. *Q. Appl. Maths* **45/3**, 583.

SIROVICH, L. 1989 Chaotic dynamics of coherent structures. *Physica* D **37**, 126.

SIROVICH, L. 1991 Analysis of turbulent flows by means of the empirical eigenfunctions. *Fluid Dyn. Res.* **8**, 85.

SIROVICH, L. & EVERSON, R. 1992 Management and analysis of large scientific datasets. *Int J. Supercomput. Applics.* **6**, 50.

SIROVICH, L., KIRBY, M. & WINTER, M. 1990 An eigenfunction approach to large scale transitional structures in jet flow. *Phys. Fluids* A **2**, 127.

SIROVICH, L., MAXEY, M. & TARMAN, H. 1989 An eigenfunction analysis of turbulent thermal convection. In *Turbulent Shear Flows 5* (ed. J.-C. André, J. Cousteix, F. Durst *et al.*), p. 68. Springer.

SIROVICH, L. & RODRIGUEZ, J. D. 1987 Coherent structures and chaos: A model problem. *Phys. Lett.* A **120**, 211.

SIROVICH, L. & SIROVICH, H. 1989 Low dimensional description of complicated phenomena. *Contemp. Maths* **99**, 277.

WHITE, R. M., COOLEY, D. S., DERBY, R. C. & SEAVER, F. A. 1958 The development of efficient linear statistical operators for the prediction of sea-level pressure. *J. Met.* **15**, 426.

WINANT, C. D. & BROWAND, F. K. 1974 Vortex pairing the mechanism of turbulent mixing layer growth at moderate Reynolds number. *J. Fluid Mech.* **63**, 237.

YANG, Z. & KARLSSON, S. K. F. 1991 Evolution of coherent structures in a plane shear layer. *Phys. Fluids* A **3**, 2207.

ZHOU, X. & SIROVICH, L. 1992 Coherence and chaos in a model of turbulent boundary layer. *Phys. Fluids* A **4**, 2855–2874.